

Studies of photoconductivity and field effect transistor behavior in examining drift mobility, surface depletion, and transient effects in Si-doped GaN nanowires in vacuum and air

N. A. Sanford, L. H. Robins, P. T. Blanchard, K. Soria, B. Klein et al.

Citation: *J. Appl. Phys.* **113**, 174306 (2013); doi: 10.1063/1.4802689

View online: <http://dx.doi.org/10.1063/1.4802689>

View Table of Contents: <http://jap.aip.org/resource/1/JAPIAU/v113/i17>

Published by the [American Institute of Physics](#).

Additional information on *J. Appl. Phys.*

Journal Homepage: <http://jap.aip.org/>

Journal Information: http://jap.aip.org/about/about_the_journal

Top downloads: http://jap.aip.org/features/most_downloaded

Information for Authors: <http://jap.aip.org/authors>

ADVERTISEMENT



AIPAdvances

Now Indexed in
Thomson Reuters
Databases

Explore AIP's open access journal:

- Rapid publication
- Article-level metrics
- Post-publication rating and commenting

Studies of photoconductivity and field effect transistor behavior in examining drift mobility, surface depletion, and transient effects in Si-doped GaN nanowires in vacuum and air

N. A. Sanford,^{1,a)} L. H. Robins,¹ P. T. Blanchard,¹ K. Soria,² B. Klein,² B. S. Eller,³
 K. A. Bertness,¹ J. B. Schlager,¹ and A. W. Sanders¹

¹*NIST, Physical Measurement Laboratory, Division 686, 325 Broadway, Boulder, Colorado 80305, USA*

²*School of Electrical and Computer Engineering, Georgia Institute of Technology, Atlanta, Georgia 30332, USA*

³*Department of Physics, Arizona State University, Tempe, Arizona 85287, USA*

(Received 26 February 2013; accepted 8 April 2013; published online 3 May 2013)

Variable intensity photoconductivity (PC) performed under vacuum at 325 nm was used to estimate drift mobility (μ) and density (σ_s) of negative surface charge for *c*-axis oriented Si-doped GaN nanowires (NWs). In this approach, we assumed that σ_s was responsible for the equilibrium surface band bending (\varnothing) and surface depletion in the absence of illumination. The NWs were grown by molecular beam epitaxy to a length of approximately 10 μm and exhibited negligible taper. The free carrier concentration (N) was separately measured using Raman scattering which yielded $N = (2.5 \pm 0.3) \times 10^{17} \text{ cm}^{-3}$ for the growth batch studied under 325 nm excitation. Saturation of the PC was interpreted as a flatband condition whereby \varnothing was eliminated via the injection of photogenerated holes. Measurements of dark and saturated photocurrents, N , NW dimensions, and dimensional uncertainties, were used as input to a temperature-dependent cylindrical Poisson equation based model, yielding σ_s in the range of $(3.5 \text{ to } 7.5) \times 10^{11} \text{ cm}^{-2}$ and μ in the range of $(850 \text{ to } 2100) \text{ cm}^2/(\text{V s})$ across the (75 to 194) nm span of individual NW diameters examined. Data illustrating the spectral dependence and polarization dependence of the PC are also presented. Back-gating these devices, and devices from other growth batches, as field effect transistors (FETs) was found to not be a reliable means to estimate transport parameters (e.g., μ and σ_s) due to long-term current drift. The current drift was ascribed to screening of the FET back gate by injected positive charge. We describe how these gate charging effects can be exploited as a means to hasten the otherwise long recovery time of NW devices used as photoconductive detectors. Additionally, we present data illustrating comparative drift effects under vacuum, room air, and dry air for both back-gated NW FETs and top-gated NW MESFETs. © 2013 AIP Publishing LLC.

[<http://dx.doi.org/10.1063/1.4802689>]

I. INTRODUCTION

Nanowires (NWs) based on GaN and related alloys have received considerable attention in recent years. Numerous device applications have been demonstrated which span a wide variety of topics such as nanomechanics, solid state lighting, chemical sensors, and optical detectors. Recent review articles offer a comprehensive look at many of these applications while new results continue to appear.^{1–4} Moreover, the NW technology offers some advantages for III-nitride based solid state lighting and commercialization efforts in this direction are apparently underway (reference to a specific company, product, or service does not constitute an endorsement by NIST).⁵

In the rapidly evolving field of NW technology, the pursuit of prototype device applications often outpaces advances in measurements of fundamental properties. Indeed, the unique 1-dimensional morphology that makes NWs so technologically attractive complicates measurements of electronic properties such as free carrier concentration (N), drift

mobility (μ), and surface band bending (SBB, \varnothing).^{6–11} Additionally, the high surface-area-to-volume ratio of NW structures may introduce surface-related effects associated with passivation and coatings, Fermi level pinning, the influence of ambient atmospheres, and surface adsorbates. Examples of such effects have previously been reported in both transient and steady-state experiments involving photoconductivity (PC), photoluminescence (PL), the behavior of NW field-effect transistors (FETs), and NW gas sensors.^{11–19} In the present work, we study transport properties, surface effects, and transient FET behavior as revealed by PC, back-gated FETs, and top-gated MESFETs. All devices were fabricated from *c*-axis GaN NWs grown by nitrogen-plasma-assisted molecular beam epitaxy (MBE).

The outline of this paper beyond the preceding introductory discussion is as follows:

- In Sec. II, we discuss NW growth and device fabrication.
- In Sec. III, we develop a temperature dependent depletion model based on solution of Poisson's equation under the assumption that the SBB is due entirely to a population of surface-trapped electrons of density σ_s . We then present results of Raman measurements performed on the NWs

^{a)}Author to whom correspondence should be addressed. Electronic mail: sanford@boulder.nist.gov

for determination of N , which is then used as an input parameter for the depletion model. Additionally, we present the results of X-ray photoelectron spectroscopy (XPS) measurements of ϕ and show in the subsequent section that the XPS-derived ϕ is consistent with the results of the depletion analysis.

- Studies of NW PC are presented in Sec. IV where we estimate σ_s , ϕ , and μ . The spectral dependence of the PC and its dependence on ambient atmosphere are also presented, and the NW diameter dependence of the polarization anisotropy of the PC is illustrated. Additionally, we show how transient gate bias effects can be exploited to hasten the otherwise slow recovery time of a photoconductive detector.
- In Sec. V, we show the limited utility of measurements of dark NW FET behavior as a means to quantify σ_s , and compare the FET results with the PC analysis of Sec. IV.
- Additional FET drift and transient phenomena are presented in Sec. VI. This includes comparisons of drift behavior in the dark and under optical excitation while in ambient conditions including vacuum, room air, and dry air.
- Discussion and conclusions are given in Secs. VII and VIII, respectively.

II. MBE GROWTH OF Si-DOPED GaN NWs AND DEVICE FABRICATION

GaN nanowires were grown on Si(111) by MBE without the use of catalysts. The NWs were c -axis oriented, Si-doped (n-type) during growth, approximately $10\ \mu\text{m}$ in length, and exhibited negligible taper. Diameters of individual NWs used in this study ranged from approximately 75 nm to 350 nm. Representative scanning electron microscope (SEM) images are shown in Figs. 1(a) and 1(b) and details of the growth procedures are described elsewhere.²⁰ This MBE growth/doping process has been shown to yield NWs with essentially axially uniform free carrier concentrations as determined by scanned electrical nanoprobe.²¹ Other characterization including photoluminescence, X-ray diffraction,

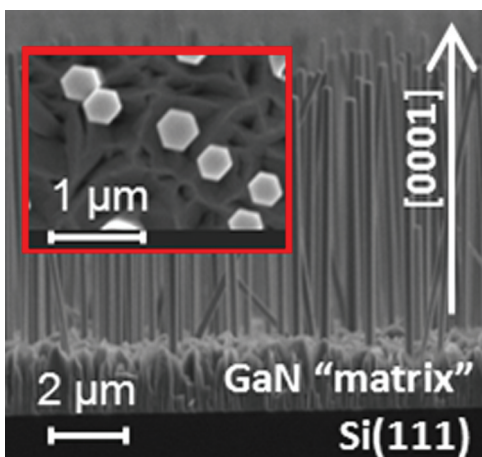


FIG. 1. (a). MBE c -axis oriented GaN NWs shown in cross section. The NWs are grown on Si(111) and emerge from a thin defective GaN “matrix” layer as described in Ref. 20. (b) Plan view image appears as the inset.

transmission electron microscopy (TEM), and nanomechanical behavior collectively support the conclusion that NWs grown in this fashion are remarkably free of structural defects and strain.¹

Nanowires were released from the growth substrate by sonication and dispersed onto the oxidized surfaces of degenerately doped Si substrates. The oxide thicknesses were nominally either 100 nm, 200 nm, or 500 nm depending on the device fabrication batch as indicated in Table I. Ohmic contacts were made to the ends of the wires as detailed elsewhere.¹¹ These contacts served as source and drain connections for back-gated FET operation, while the gate contacts were made directly to the silicon substrates. Examples of a back-gated NW FET, and a top-gated NW MESFET, are illustrated in Figs. 2(a) and 2(b), respectively. The NW MESFETs used in this study were described earlier.¹⁷ All devices were carefully checked for electrical shorting paths through the oxide film; devices exhibiting shorts were excluded from the results. Dimensional details of the samples used in the present work appear in Table I.

III. COMPUTATION OF NW DEPLETION IN THE DARK

A. Cylindrical depletion model

The geometry of our cylindrical depletion model is illustrated schematically in Fig. 3(a). We envision an equilibrium scenario whereby a uniform density σ_s of negatively charged (occupied) surface traps reside below the Fermi level, as illustrated. A distribution of neutral hole traps is also assumed as indicated. It is also likely that a distribution of empty traps for either charge type extends above the Fermi level and we illustrate such an empty electron trap. For brevity, other presumed empty hole traps, or neutral traps, are omitted. The trapped electrons on the NW surface induce band bending and produce a radially varying free carrier concentration (n) and a radially varying potential (V) which are both functions of the radial coordinate (r). The radial dependence of the conduction band energy is given by $E_c = -qV$, where q is the magnitude of the fundamental charge and the energy is referenced such that $E_c = 0$ is the position of the conduction band edge in the absence of depletion. Note that the sign of V is negative so that the sense of the SBB is upward. In the absence of illumination, $\phi = E_c(r_A) - E_c(0)$, where r_A is the radius of the cylinder representing the NW as described below. We avoid use of the more simplified abrupt depletion approximation that is oftentimes adopted (Refs. 2 and 6–11) because it is inaccurate for cases approaching significant depletion.¹¹

V was calculated by solving Poisson’s equation in cylindrical coordinates under the assumptions that donors of density n_b are fully ionized and uniformly distributed throughout the NW, no free holes or ionized acceptors are present, and Boltzmann statistics apply.²² With the substitutions $v = qV/kT$ and $n = n_b e^v$, one obtains

$$\frac{d^2v}{dr^2} + \frac{1}{r} \frac{dv}{dr} = \frac{-q^2}{\kappa \epsilon_0 kT} n_b (1 - e^v). \quad (1)$$

In the preceding equation, the dielectric constant $\kappa = 8.9$, k is the Boltzmann’s constant, T is the absolute temperature, and

TABLE I. Summary of samples used in the present study. The abbreviations “PC/FET/pol” refer to the sample used for photoconductivity, FET, or polarization-dependent photoconductivity experiments. Samples used in experiments involving spectral dependence of PC are noted by “spec”. L and D_m are defined in the text and illustrated in Figs. 2(a) and 3(b), respectively. All samples were dispersed onto oxidized Si substrates with oxide thicknesses given in column 5. “BG” and “TG” refer to back gated or top (Schottky) gated FET configurations, respectively. L_g is the length of the gate contact that overlaps the NW for TG devices as illustrated in Fig. 2(b). Sample die from growth batches C236 and B982 is listed in column 7. As described in the text, we assume that the free carrier concentration N as measured by Raman scattering is equivalent to the Si doping density n_b for these two batches as indicated.

Sample	PC/FET/pol	D_m (nm)	L (μm)	oxide (nm)	BG/TG, L_g (μm)	Batch/die
C236 $n_b = (2.5 \pm 0.3) \times 10^{17} \text{cm}^{-3}$						
1	PC, pol, FET	75	3.3	500	BG	2133WQ D16 I-2-8
2	pol, spec	76	3.3	200	BG	23732WB D5 III-4-2
3	PC, pol FET	79	3.0	500	BG	2133WQ D16 III-1-6
4	PC, FET	80	3.4	200	BG	23732WB D6 III-1-4
5	FET	83	3.4	200	BG	23732WB D6 I-7-4
6	PC, FET	84	3.8	200	BG	23732WB D6 I-5-3
7	spec	90	3.7	200	BG	23732WB D5 II-7-3
8	PC, pol, FET	90	3.7	500	BG	2133WQ D16 III-5-3
9	FET	94	3.3	200	BG	23732WB D6 I-7-3
10	PC, pol FET	101	3.9	500	BG	2133WQ D16 II-6-7
11	FET	128	4.5	200	BG	23732WB D6 III-5-6
12	PC, FET	129	5.4	500	BG	2133WQ D16 IV-5-6
13	PC, pol	139	3.5	500	BG	2133WQ D16 II-2-7
14	PC	148	3.4	500	BG	2133WQ D16 II-2-5
15	PC	157	3.6	200	BG	23732WB D6 III-8-6
16	FET	176	3.2	200	BG	23732WB D5 I-4-3
17	PC, pol	194	3.5	500	BG	2133WQ D16 II-5-5
18	FET	220	4.0	200	BG	23732WB D6 II-8-7
B982 $n_b = (1.2 \pm 0.2) \times 10^{17} \text{cm}^{-3}$						
19	PC, FET	372	4.4	100	BG	TiAl T53 III-5-2
20	FET	238	3.5	100	BG	TiAl T53 I-3-3
21	FET	353	8.0	600	TG, 3.0	A2 I-5-6
22	FET	188	7.4	600	TG, 3.4	A2 II-5-3

r is the radial coordinate. The geometry is illustrated in Fig. 3(b) where the cylinder diameter D_A is chosen such that the cross-sectional area A is equivalent to that of a hexagon with diagonal of length D_m parallel to $\langle 11\bar{2}0 \rangle$. Hence, $D_A \approx 0.91D_m$ and $r_A = D_A/2$. Equation (1) is solved using standard Runge-Kutta methods.²³ Numerical integration of n over the cross-section of the NW yields Q_i^D which is the free charge per unit length (in the dark). The source-drain current in the dark I_{sd}^D then becomes

$$I_{sd}^D = q\mu Q_i^D V_{sd}/L, \quad (2)$$

where V_{sd} , L , and μ are the source-drain voltage, electrode gap, and drift mobility, respectively. We remark that the cylindrical Poisson solver was further validated by considering charge neutrality via $n_b D_A/4 - Q_i^D/\pi D_A = \sigma_s$ which was obeyed within computational round-off error for numerous cases checked.

The estimated uncertainty in NW diameter $\delta D_m = \pm 5 \text{ nm}$. The extremal values of D_m are given by $D_m^\pm = D_m \pm \delta D_m$ with corresponding $D_A^\pm = D_A \pm \delta D_A$. Taking δD_m into account, our cylindrical approximation yielded results for Q_i^D that bracketed those obtained from a finite-element solver applied to an idealized NW of hexagonal cross section where the same values of n_b and σ_s were used in both cases. Therefore, given its overall computational convenience, we regard the cylindrical approximation as adequate for simulation of dark depletion in a 2-terminal

NW device. However, as discussed in Sec. V, analysis of depletion in back-gated FET NW devices required use of the finite-element solver since cylindrical symmetry was absent.

B. Measurements of free carrier concentration by Raman analysis

Raman scattering provides a means to determine the free carrier concentration N by measuring the frequency shift of the coupled longitudinal-phonon-plasmon (LPP+) mode. Raman scattering with 633 nm excitation was performed in ambient air on dense as-grown NW ensembles. The focused laser spot had dimensions of $\approx (2.4 \times 1.0) \mu\text{m}$, and the excitation density was in the range of (25 to 95) kW/cm^2 for all Raman measurements. More details of the Raman work applied to GaN nanowires were given elsewhere and will also appear in an upcoming article.²⁴

To insure that depletion did not reduce the density of free carriers to render an artificially low value of N , the Raman studies were repeated with co-illumination by a 325 nm (above GaN bandgap) cw UV HeCd laser with spot size of $(250 \times 460) \mu\text{m}$, and a filter-selectable excitation intensity of 0.7 W/cm^2 or 4.5 W/cm^2 . We know from results present below, and prior studies (Refs. 10 and 11), that above-gap excitation at this intensity should substantially reduce or eliminate depletion in single NWs. For as-grown NW ensembles from batch C236, no additional shift in the LPP+ mode or other Raman modes was observed under

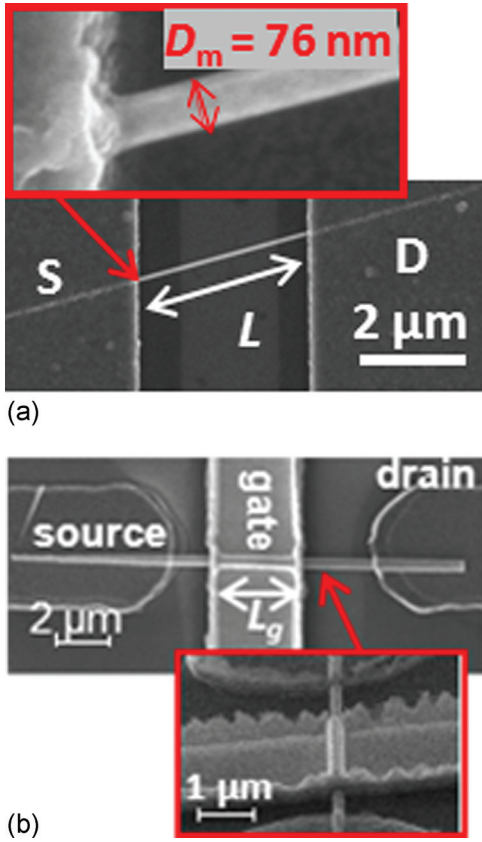


FIG. 2. (a) FESEM image of sample 2 illustrating typical back gated FET configuration. (b) Image of typical MESFET sample.

simultaneous 632 nm and UV nm illumination. However, small UV-induced shifts in the LPP+ mode were observed in batch B982 and several other NW batches (B738, C023, C144, and N365). The LPP+ peak was narrower and more intense in batches excluding C236, thus UV induced shifts

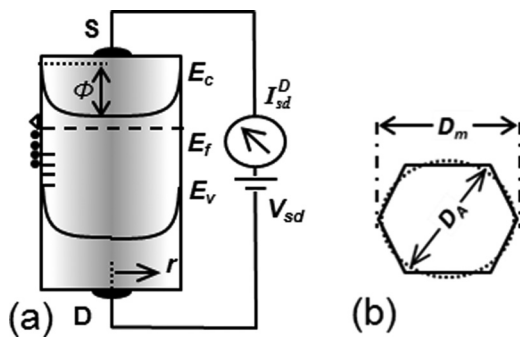


FIG. 3. (a) Model schematic of trapped electrons of surface density σ_s producing upward band bending ϕ in a cylindrical NW of diameter D_A . The radial coordinate r is indicated with $r_A = D_A/2$. In the scenario illustrated, electrons occupying surface traps, and empty neutral hole traps, residing below the Fermi level are indicated by the respective symbols “•” and “-”. An empty electron trap above the Fermi level is shown as “Δ”. Cylindrical symmetry is assumed and the preceding symbols only appear on the left side of the figure for brevity. Conduction band, Fermi level, and valence band are labeled by E_c , E_f , and E_v , respectively. The radial gradient in the shading and curvature of the bands indicates that the depletion is minimal in the vicinity of $r = 0$ and increases as $r \rightarrow r_A$. With the device in the dark, source-drain voltage V_{sd} produces current I_{sd}^D as indicated. (b) Cylinder of diameter D_A representing an idealized hexagonal NW. D_m is the separation between extreme hexagonal vertices is as shown. D_A is chosen such that the cylinder and hexagon have the same cross sectional area as described in the text.

were more readily observable. Excluding batch C236, the average upshift in the LPP+ peak under 0.7 W/cm^2 UV co-illumination was $(0.11 \pm 0.12) \text{ cm}^{-1}$. From our model describing the dependence of LPP+ frequency on N , this shift corresponds to an increase in free carrier concentration of $(4 \pm 5) \times 10^{15} \text{ cm}^{-3}$.

We conclude from the studies performed under UV co-illumination that the Raman scattering primarily sampled the thicker NWs where photo-induced variations in depletion thickness were minor perturbations, or that the depletion was substantially reduced by the intense ($25\text{--}95 \text{ kW/cm}^2$) 632 nm excitation such that simultaneous UV excitation had little additional effect. Indeed, as described in Sec. IV, below-gap visible excitation is effective in reducing depletion. Furthermore, since the absorption depth for GaN at 325 nm is $\approx 80 \text{ nm}$ (Ref. 11), it is reasonable to assume that the UV excitation perturbed the SO mode more than the LPP+ mode since the SO mode primarily samples the NW surface. Analysis of the Raman measurements of the LPP+ frequency (without UV co-illumination) yielded $N \pm \delta N = (2.5 \pm 0.3) \times 10^{17} \text{ cm}^{-3}$ for batch C236 and $N \pm \delta N = (1.2 \pm 0.2) \times 10^{17} \text{ cm}^{-3}$ for batch B982. These values are also indicated in Table I.

C. Measurements of SBB via XPS

XPS analysis was used to measure the SBB on as-grown air-exposed NW ensembles from batch C236. We denote the XPS derived value of SBB as ϕ_{xps} . Our basic approach for XPS studies of GaN surfaces has been given elsewhere.²⁵ XPS revealed that the samples supported a significant level of carbon contamination that could be removed using various *in situ* plasma treatments within the UHV XPS system. However, since the case of present interest only involves air-exposed NWs that have had no post-growth cleaning or encapsulation which would render contamination-free surfaces, we only give results for as-received air-exposed samples.

The binding energy of the Ga3d core level $E_{\text{Ga-3d}}$ was measured with respect to the Fermi level yielding 20.9 eV. Using this and the results of Ref. 26 giving $E_v - E_{\text{Ga-3d}} \approx 17.8 \text{ eV}$, the Raman-derived value of N (with the implicit approximation $N \approx n_b$) and standard methods for calculating the position of the Fermi level with respect to conduction and valence bands (Ref. 27), we find that $E_f - E_v = (3.1 \pm 0.1) \text{ eV}$ and $\phi_{xps} = (0.2 \pm 0.1) \text{ eV}$. For the same NW samples subjected to *in-situ* plasma cleaning and annealing within the XPS chamber as detailed in Ref. 25, the SBB was larger than in ambient air: $E_f - E_v = (2.8 \pm 0.1) \text{ eV}$ and $\phi_{xps} = (0.5 \pm 0.1) \text{ eV}$.

D. Examples of NW depletion in the cylindrical approximation

With experimental results (and uncertainties) for n_b and ϕ_{xps} in hand (under the assumption that $N \approx n_b$), it is instructive to simulate depletion for several hypothetical cases of D_A . Setting $T = 295 \text{ K}$, $n_b = 2.5 \times 10^{17} \text{ cm}^{-3}$ and choosing $\sigma_s = 4.9 \times 10^{11} \text{ cm}^{-2}$, solutions of Eq. (1) for n and E_c are shown in Fig. 4(a) for $79 \text{ nm} < D_A < 200 \text{ nm}$. As D_A

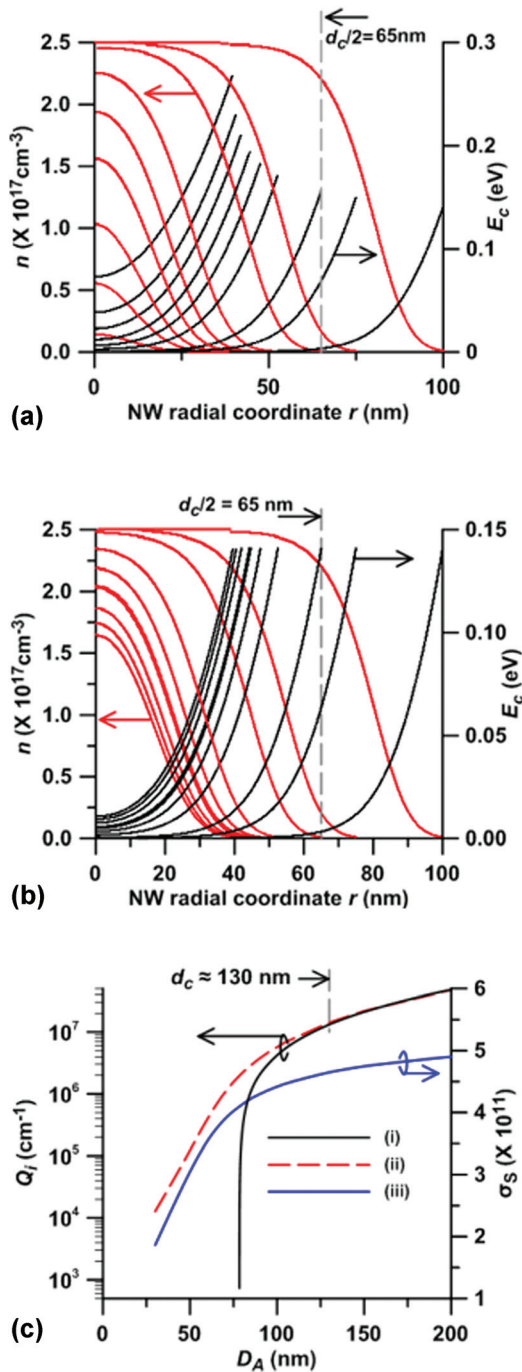


FIG. 4. (a) Case of assumed constant surface charge density σ_s : Graphs of n (red) and E_c (black) as functions of r for values of $D_A = 79, 81, 84, 89, 95, 105, 130, 150,$ and 200 nm . $T = 295 \text{ K}$, $n_b = 2.5 \times 10^{17} \text{ cm}^{-3}$, and $\sigma_s = 4.9 \times 10^{11} \text{ cm}^{-2}$ throughout. The NW at the critical diameter d_c corresponds to $D_A \approx 130 \text{ nm}$ where $n(0)$ just falls below n_b . (b) Case of assumed constant surface potential ϕ_S : Graphs of n (red) and E_c (black) as functions of r for same set of D_A as used in (a). $T = 295 \text{ K}$, $n_b = 2.5 \times 10^{17} \text{ cm}^{-3}$, and $\phi_S = 0.21 \text{ eV}$ throughout. This case also illustrates that $d_c \approx 130 \text{ nm}$. (c) Graph (i) shows integrated charge Q_i^D as a function of D_A for $30 \text{ nm} < D_A \leq 200 \text{ nm}$ with values of T , n_b , and σ_s used in (a). Graph (ii) shows Q_i^D as a function of D_A over the same span of diameters with values T , n_b , and ϕ_S used in (b). Graph (iii) shows the diameter dependence of σ_s resulting from the computation of graph (ii).

decreases from 200 nm to 130 nm, depletion penetrates further into the NW but $n(0)$ and ϕ remain $\approx n_b$ and $\approx 0.14 \text{ eV}$, respectively. As D_A decreases further from 130 nm to 79 nm, depletion increasingly extends into the entire NW with

$n(0) < n_b$, $E_c(0) > 0$, and $\phi > 0.14 \text{ eV}$. The value of D_A at which the depletion just penetrates to the NW center has been called the “critical diameter” (Refs. 2, 7, and 8) which we label as d_c . Figure 4(a) illustrates that $d_c \approx 130 \text{ nm}$ for the hypothetical cases considered.

Using n_b and tabulated parameters for GaN, one may calculate by standard methods (Ref. 27) that the Fermi level E_f falls roughly 0.07 eV below $E_c = 0$. Hence, by postulating σ_s is a constant, the surface potential $\phi_S \equiv E_c(r_A) - E_f$ is not a constant over this range of D_A but varies from roughly 0.34 eV to 0.21 eV. Clearly, only surface states that fall below or within kT of E_f can contribute to σ_s but the actual distribution of these levels (above and below E_f) is unknown. Since the estimated uncertainty in ϕ_{xps} is $\pm 0.1 \text{ eV}$, there is no loss in generality in assuming a constant value of σ_s over the range of D_A considered. Nonetheless, we next assume that ϕ_S is constant regardless of NW diameter and explore the numerical consequences of that assumption.

In Fig. 4(b), we consider the same values of D_A , n_b , and T used in Fig. 4(a) and illustrate the solutions for n and E_c assuming constant surface potential with $\phi_S = 0.21 \text{ eV}$. In this case, we also find $d_c \approx 130 \text{ nm}$. However, inspection of Figs. 4(a) and 4(b) reveals that for $D_A < d_{crit}$ the dependence of Q_i^D on D_A , and hence the expected trend in conductivity, is quite different for the two cases. For example, in Fig. 4(c), the dependence of Q_i^D on D_A is compared for the constant- σ_s and constant- ϕ_S conditions, with $30 \text{ nm} < D_A < 200 \text{ nm}$. For constant σ_s , these simulations indicate that NWs with $D_A < 78 \text{ nm}$ should be substantially depleted—which is, in fact, observed experimentally for batch C236. On the other hand, the constant- ϕ_S simulation shows that the wires should be out of depletion even at the 30 nm lower limit of D_A . Figure 4(c) also shows the dependence of σ_s on D_A that accompanies the assumption of constant- ϕ_S .

Since the actual measured quantity is I_{sd}^D rather than Q_i^D , further complications may arise due to the likely dependence of μ on D_A for the thinner NWs, i.e., low conductivity observed in NWs with relatively small diameters being attributed to increased depletion when reduced mobility due to side-wall scattering may actually be the dominant effect. However, as described in the Appendix, we estimate that a reduction of μ with decreasing D_A should not be significant until D_A falls below $\approx 76 \text{ nm}$. Therefore, even with the dependence of μ on D_A taken into consideration, it is not clear whether the assumption of constant σ_s or the assumption of constant ϕ_S is the more applicable interpretation of these experiments. These points are considered further in Sec. VII, where we compare our results with other reports.

IV. PC STUDIES

A. Dark conductivity and PC under vacuum to estimate μ , σ_s , and ϕ

We define P_i^λ as the cw illumination intensity at wavelength λ and λ_{ag} as the above-gap wavelength within the available UV range $325 \text{ nm} < \lambda < 360 \text{ nm}$. Excitation of a NW with $P_i^{\lambda_{ag}}$ produces photogenerated holes which drift to the surface whereupon they may become trapped and/or recombine with trapped electrons. Consequently, the SBB

falls to ϕ_p (with $\phi_p < \phi$), the depletion is reduced, and the integrated free charge in the NW increases. Hence, for constant V_{sd} , the source-drain current under illumination I_{sd}^P (the photocurrent) is greater than I_{sd}^D . This situation remains in a state of dynamic equilibrium under continuous illumination with a recombination current of electrons and holes flowing to the surface. With the illumination removed the initial dark equilibrium condition is eventually restored via thermally excited electrons surmounting ϕ and becoming trapped on the surface and/or recombining with trapped holes. This process is illustrated schematically in Fig. 5.

A cw HeCd laser operating at 50 mW was attenuated using an assortment of UV neutral density filters and thus formed a variable-intensity source for P_i^{325} . With P_i^{325} sufficiently high, $\phi_p \rightarrow 0$ resulting in the saturated photocurrent $I_{sd}^S = q\mu n_b AV_{sd}/L$. Measurement of I_{sd}^S permitted the calculation of μ since all other terms in the preceding equation are separately known. The onset of photocurrent saturation with increasing P_i^{325} is illustrated in Fig. 6(a) for sample 15 (under vacuum) with $V_{sd} = 20$ mV, and $40 \mu\text{W cm}^{-2} < P_i^{325} < 390 \text{ W cm}^{-2}$. Using extremal values $D_m = D_m^\pm$ and $n_b = n_b^\pm$ in the analysis, we calculate the corresponding low and high values for mobility $\mu^- \approx 1490 \text{ cm}^2/(\text{V s})$ and $\mu^+ \approx 2100 \text{ cm}^2/(\text{V s})$, which were required to reconcile the measured I_{sd}^S . Figure 6(b) gives a summary for a collection of 11 such NW devices with $75 \text{ nm} < D_m < 195 \text{ nm}$. These correspond to samples labeled ‘‘PC’’ within the C236 batch as summarized in Table I. Note that the data in Fig. 6(b)

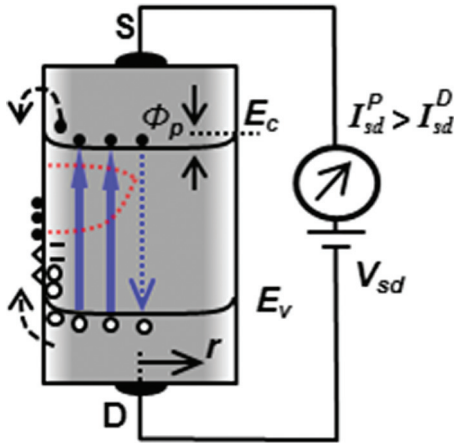


FIG. 5. Model schematic of NW excited above bandgap indicated by upward arrows. Conduction band to valence band recombination indicated by downward dashed arrow. Photogenerated holes, indicated by ‘‘o’’ symbols, drift to the surface, become trapped, accumulate near the valence band maximum, and/or recombine with trapped electrons. $\phi \rightarrow \phi_p$ as the net negative surface charge is reduced. Resulting neutral electron traps are indicated by ‘‘Δ’’ symbols. Steady illumination produce recombination current that flows to the surface since electrons in the interior of the NW now see the reduced barrier ϕ_p where $\phi_p < \phi$ the latter of which appears in Fig. 3(a). Radial symmetry is assumed with the surface charges and traps illustrated only on one side of the figure and effective Fermi levels for electrons and holes intuitively indicated by the dashed red lines which converge near $r = 0$. The source-drain voltage V_{sd} now produces current I_{sd}^P with $I_{sd}^P > I_{sd}^D$ the latter of which was shown in Fig. 3(a). The radial gradient in the shading indicates that the depletion is reduced from that shown in Fig. 3(a). With the illumination ceased, dark equilibrium is eventually restored via electrons surmounting the surface barrier and becoming trapped on the surface and/or recombining with holes trapped or accumulated near the surface.

suggest no dependence of mobility on NW diameter. Taken together, the results indicate a fairly high uncertainty in the computed values of mobility with μ spanning over roughly 800–2100 $\text{cm}^2/(\text{V s})$. The data used to generate these results were recorded under vacuum (mid- 10^{-6} Torr).

We compute σ_s as follows. Using measured quantities I_{sd}^D , V_{sd} , and L , in conjunction with the respective D_A^\pm , n_b^\pm , and μ^\pm , iteration of Eqs. (1) and (2) yields the corresponding high and low values σ_s^\pm of surface charge density and associated graphs for n and E_c . In this context, it is understood that I_{sd}^D refers to steady-state dark current. An example of this analysis is shown in Fig. 7(a) for sample 10 with $D_m = 101 \text{ nm}$. Figure 7(a) shows the results for $D_A^+ = 106 \text{ nm}$, $n_b^+ = 2.8 \times 10^{17} \text{ cm}^{-3}$, and $\mu^- = 900 \text{ cm}^2/(\text{V s})$, which yields $\sigma_s^+ = 5.4 \times 10^{11} \text{ cm}^{-2}$, and $\phi \approx 0.18 \text{ eV}$. Figure 7(a) also illustrates the opposite extreme where $D_A^- = 96 \text{ nm}$, $n_b^- = 2.2 \times 10^{17} \text{ cm}^{-3}$, and $\mu^+ = 1300 \text{ cm}^2/(\text{V s})$, which yields $\sigma_s^- = 3.8 \times 10^{11} \text{ cm}^{-2}$, and $\phi \approx 0.13 \text{ eV}$. Figure 7(b) gives a summary of this analysis performed on the same set of 11 samples described in Fig. 6(b). The uncertainties in the computed values σ_s fall into the range of $1.5\text{--}2.0 \times 10^{11} \text{ cm}^{-2}$ for all cases. The dashed curve in Fig. 7(b) is a polynomial fit to the average value of σ_s^\pm , i.e., $(\sigma^+ + \sigma^-)/2$, for each sample. The trend illustrates that there may, in fact, be a dependence of σ_s

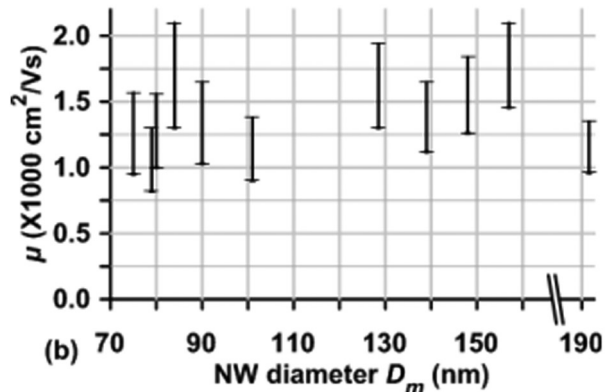
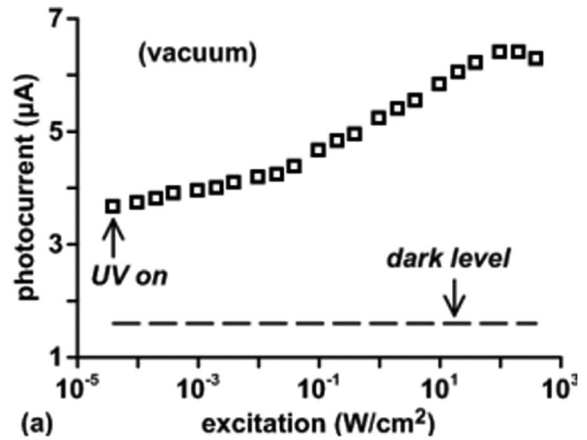


FIG. 6. (a) Photocurrent I_{sd}^P recorded under vacuum on sample 15 for $V_{sd} = 20$ mV and $40 \mu\text{W cm}^{-2} < P_i^{325} < 390 \text{ W cm}^{-2}$. The dark level prior to any UV excitation is also shown. (b) Extremal values μ^\pm calculated from saturated photocurrent I_{sd}^S as described in the text. The results were compiled from measurements performed on samples labeled ‘‘PC’’ within the C236 batch as summarized in Table I.

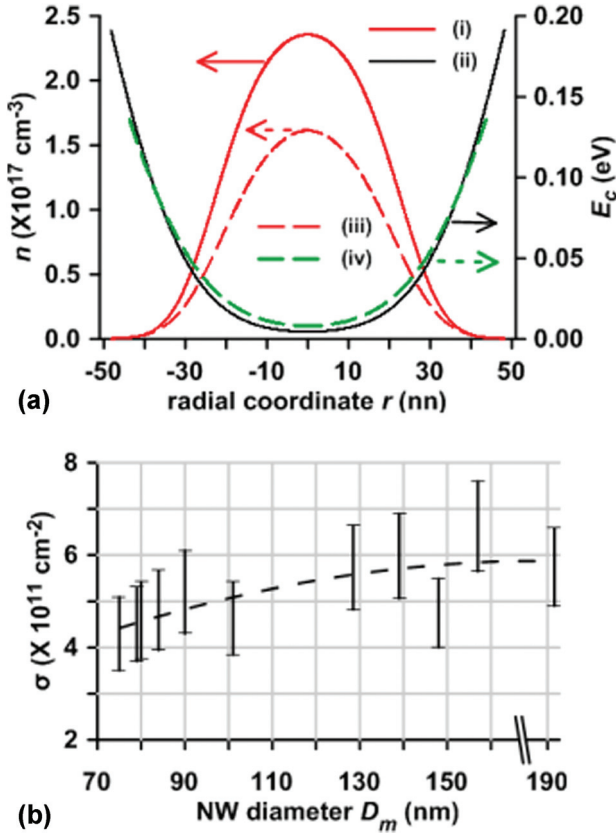


FIG. 7. (a) Computed n and E_c across full NW diameter for sample 10 yielding extremal values σ_s^\pm that reconcile the measured I_{sd}^D when μ^\pm and uncertainties δD_A and δn_b are taken into account. In graphs (i) and (ii), $D_m^+ = 106 \text{ nm}$, $n_b^+ = 2.8 \times 10^{17} \text{ cm}^{-3}$, and $\mu^- = 900 \text{ cm}^2/(\text{V s})$. This yields $\sigma_s^+ = 5.4 \times 10^{11} \text{ cm}^{-2}$ and $\varnothing \approx 0.18 \text{ eV}$. In graphs (iii) and (iv), $D_m^- = 96 \text{ nm}$, $n_b^- = 2.2 \times 10^{17} \text{ cm}^{-3}$, and $\mu^+ = 1300 \text{ cm}^2/(\text{V s})$. This yields $\sigma_s^- = 3.8 \times 10^{11} \text{ cm}^{-2}$, and $\varnothing \approx 0.13 \text{ eV}$. (b) Extremal values σ_s^\pm calculated as described in the text for samples labeled “PC” within the C236 batch as summarized in Table I. The dashed line is a polynomial fit to the average values of σ_s^\pm , i.e., $(\sigma^+ + \sigma^-)/2$, for each sample.

on D_m as suggested in Sec. III D above. However, the computed values for \varnothing fall within the uncertainty of the XPS measurements, uncertainties in the other pertinent quantities are relatively high, and more samples, and samples with different doping levels, are required in order to perform a stronger statistical analysis. Nonetheless, if the trend of diminishing σ_s with reduced D_m is indeed correct, then the physical situation is best described by a model postulating constant ϕ_s . As described in Sec. VII below, this picture would help reconcile reports of different NW PC studies which collectively describe comparable values of \varnothing over wide range of doping densities.

The polarization anisotropy of the PC was examined since reports indicate (Refs. 28 and 29) that the photocurrent $I_{sd}^{P\parallel}$ for the optical polarization aligned parallel to the NW axis ($\theta = 0^\circ$) should be greater than for photocurrent $I_{sd}^{P\perp}$ arising from the orthogonal polarization ($\theta = 90^\circ$). With $I^{Rm} \equiv I_{sd}^{P\perp}/I_{sd}^{P\parallel}$ and $I^{R(\theta)} \equiv I_{sd}^{P(\theta)}/I_{sd}^{P\parallel}$, Fig. 8 illustrates approximately that $0.9 < I^R \leq 1.0$ for samples (labeled “pol” in Table I) with $75 \text{ nm} \leq D_m \leq 194 \text{ nm}$. Thus, although resolvable in the thinnest NW device samples available to us, polarization anisotropy of the PC did not introduce significant additional uncertainty into measurements of I_{sd}^P or I_{sd}^S . This is consistent with our earlier work on devices with D_m

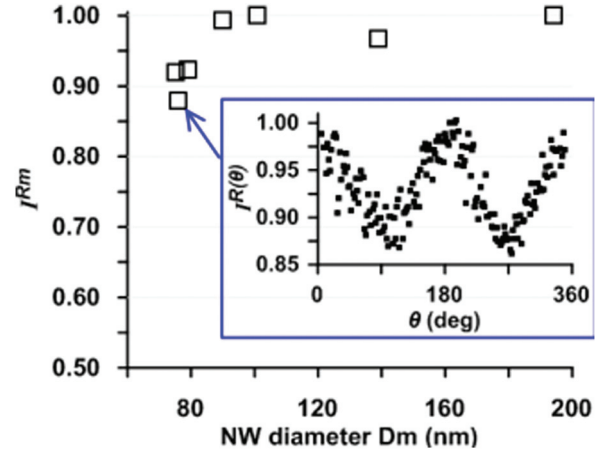


FIG. 8. Maximum polarization anisotropy of photocurrent I^{Rm} for samples labeled “pol” in Table I. Inset: angular dependent polarization anisotropy of photocurrent $I^{R(\theta)}$ for sample 2.

$> 100 \text{ nm}$ made from separate growth batches where PC anisotropy effects were not observed.¹¹

B. Influence of ambient atmosphere on dark conductivity and PC

We examined dark conductivity and PC in room air, dry air, and vacuum. I_{sd}^D was essentially the same in either air ambient. However, I_{sd}^D under vacuum was always greater than in air. This suggests adsorbed oxygen and/or hydrogen species contribute to σ_s and may be at least partially desorbed under vacuum. UV exposure under vacuum produced higher I_{sd}^S than UV exposure in air which is evidence for photo-induced desorption of surface species in addition to the apparent desorption under vacuum. With the UV blocked, PC decay under vacuum revealed that even after several days I_{sd}^D would not fall to the level recorded prior to UV illumination. However, upon re-introduction of air in the dark, I_{sd}^D would rapidly drop to the original value observed in air. To avoid cluttering the notation, we refrain from defining an additional variable that specifically labels the time dependence of I_{sd}^D since this should be evident within the context of the discussion and the related graphical results.

Figure 9(a) illustrates these effects for sample 10. Figure 9(b) shows σ_s^\pm computed for I_{sd}^D in vacuum and air prior to UV exposure, and σ_s^\pm after several days of PC decay in vacuum. Apparent UV and vacuum induced desorption effects similar to those illustrated here have been reported for GaN films studied by surface photovoltage methods and for GaN nanowires used for gas sensing.^{4,12,30}

C. Spectral dependence of PC in vacuum and air

The spectral dependence of the PC within a tunable range from 360 nm to 550 nm was explored using a source composed of a 75 W Xe arc lamp dispersed by a monochromator. The spectrally tunable output was then directed into the vacuum probe station through a fused quartz window using various bulk optics and a liquid-filled light guide. The spectral bandwidth delivered to the sample was roughly 5 nm and P_i^2 remained within a factor of 2 of $\approx 0.2 \text{ mW/cm}^2$ over

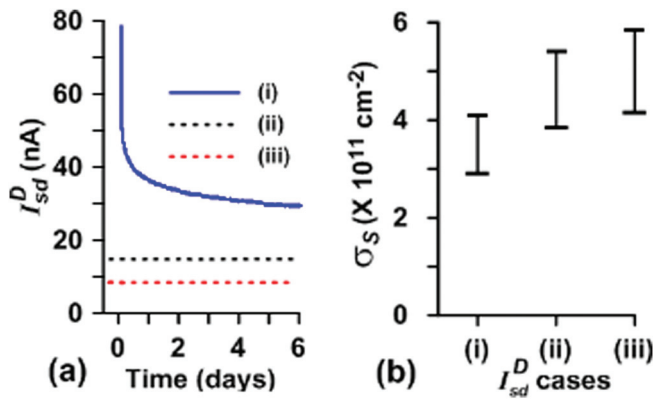


FIG. 9. (a) Comparison of dark current I_{sd}^D for sample 10, with $V_{sd} = 10$ mV, for the following conditions: (i) decay of I_{sd}^D under vacuum after initial excitation of $P_i^{325} = 390$ W/cm²; (ii) I_{sd}^D in vacuum prior to UV excitation; (iii) I_{sd}^D in room air prior to UV excitation. (b) Extremal values σ_s^\pm calculated for the 3 cases of I_{sd}^D illustrated in (a). For case (i), σ_s^\pm are given for I_{sd}^D after 6 days have elapsed.

the spectral range indicated. The tunable PC response was most pronounced for $\lambda \approx 360$ nm and weakened sharply as λ extended into the visible.^{11,29} The mechanism for sub-gap PC is not well established but likely involves a reduction in σ_s via photoexcitation of electrons out of surface states, or sub-gap traps near the surface.^{31,32} The sensitivity of PC under visible excitation depends upon the degree of NW depletion as follows. If the NW is essentially depleted $I_{sd}^D \approx 0$ and the sub-gap excitation for $P_i^\lambda \approx 0.2$ mW/cm² is ineffective in reducing σ_s enough to substantially increase I_{sd}^P out of the noise. However, excitation near 360 nm is heavily absorbed and produces a significant population of photogenerated holes that reduce σ_s resulting in $I_{sd}^P \gg I_{sd}^D$. If the NW is not depleted $I_{sd}^D > 0$ and the relatively small perturbation in σ_s induced by sub-gap excitation nevertheless results in I_{sd}^P which can typically be detected above I_{sd}^D .

These effects are illustrated in Fig. 10(a) where the spectral dependence of PC in vacuum and air is shown for sample 2 with $D_m = 76$ nm. Under vacuum, the device is out of depletion and the PC sensitivity extends into the visible. In air, I_{sd}^P rolls off sharply for $\lambda > 360$ nm and goes into the noise for $\lambda \approx 425$ nm. Figure 10(b) illustrates the case for sample 7 with $D_m = 90$ nm. In this case, the device is out of depletion in both air and vacuum. Of course, it is quite likely that visible excitation intensities $\gg 0.2$ mW/cm² will induce significantly greater conductivity than reported herein for an otherwise depleted NW, but this was not explored in the present work.

D. Demonstration of method to “reset” the photoconductive response

The above-gap PC response is characterized by a rapid increase in conductivity upon excitation followed by some characteristic decay time to recover the equilibrium value of I_{sd}^D after the light is blocked. PC decay times can vary considerably depending upon the degree of depletion and ambient conditions. For example, Fig. 11 compares the photocurrent I_{sd}^P and the decay of I_{sd}^D recorded for sample 2 after excitation with $P_i^{360} \approx 0.2$ mW/cm² in air and vacuum,

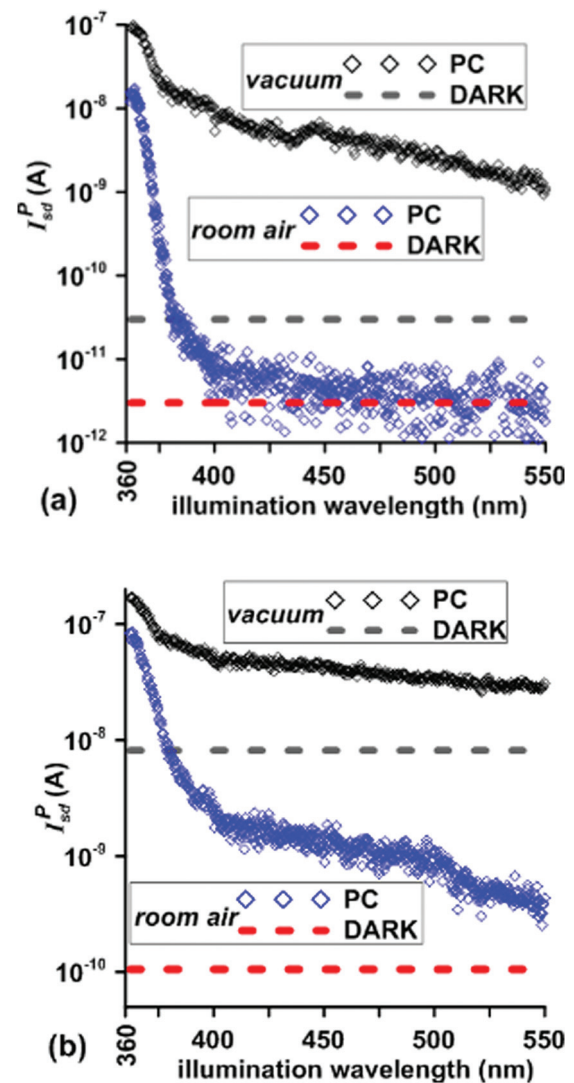


FIG. 10. (a) Comparative spectral dependence of PC for sample 2 ($D_m = 76$ nm) in air and vacuum with and $P_i^\lambda \approx 0.2$ mW/cm² over the 360–550 nm wavelength range. $V_{sd} = 200$ mV for both cases. The NW diameter is chosen to illustrate that for the excitation conditions given, the PC is nonzero in vacuum over the entire wavelength range but falls into the noise near 425 nm in room air. Apparent feature near 450 nm for the case under vacuum is an instrumental artifact. (b) Comparative spectra dependence of PC for sample 7 ($D_m = 90$ nm) in air and vacuum over the same wavelength range and excitation conditions as in (a). In this case, the thicker NW is out of depletion in both air and vacuum. $V_{sg} = 100$ mV for both cases.

respectively. Operating under vacuum produces roughly $10\times$ greater I_{sd}^P than in room air for this particular sample but the time for I_{sd}^D to reach equilibrium under vacuum is roughly 20 h compared to only few minutes in room air. Therefore, a scheme to “reset” the photoconductor, i.e., rapidly restore I_{sd}^D to a minimum value, would be quite useful for the practical implementation of such devices for optical detectors.

A model for the reset procedure for a NW photoconductor configured as a back-gated FET is illustrated schematically in Figs. 12(a)–12(f). Labels \emptyset , \emptyset_p , and V_{sd} are omitted for clarity but are implicitly consistent with Figs. 3(a) and 5. Symbolic designation of electrons, holes, traps, and quasi Fermi levels is also consistent with the prior figures. The operational sequence is as follows: (a) The device

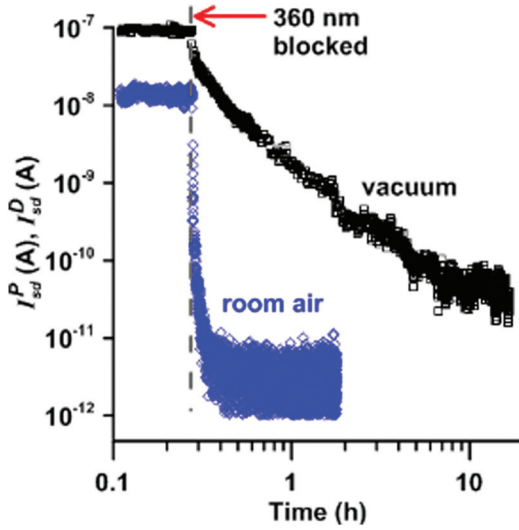


FIG. 11. Comparative photocurrent I_{sd}^P under $P_i^{360} \approx 0.2 \text{ mW/cm}^2$, and decaying dark current I_{sd}^D in room air and vacuum for sample 2. $V_{sd} = 200 \text{ mV}$ for both cases.

is initially in a dark equilibrium state with $\text{SBB} = \emptyset$, $V_{sg} = 0$, $V_{sd} \neq 0$, and $I_{sd} = I_{sd}^D$. (b) Keeping $V_{sg} = 0$ and illuminating with $P_i^{360} > 0$, the SBB falls to \emptyset_p resulting in $I_{sd}^P > I_{sd}^D$. (c) Keeping $V_{sg} = 0$ but setting $P_i^{360} = 0$, results in both I_{sd}^D and \emptyset decaying relatively slowly back toward their respective initial dark states. (d) Keeping $P_i^{360} = 0$ but setting V_{sg} to some fixed negative voltage produces an accumulation condition whereby $\emptyset < 0$, I_{sd}^D rises to some maximum value which is greater than I_{sd}^D observed in (b). Conduction electrons flood surface traps since the sign of the surface barrier is now reversed. (e) Keeping $P_i^{360} = 0$ but setting V_{sg} back to zero results initially in \emptyset greater and I_{sd}^D less than their respective values in (a) since electron traps are now filled which reside at a higher energy than the Fermi level in the quasi neutral region of the NW. (f) With P_i^{360} and V_{sg} both zero, the conditions described in (a) are eventually recovered as the surface trapped electrons return to equilibrium with the NW

Figure 13(a) demonstrates the reset sequence implemented under vacuum on sample 11 with $V_{sd} = 50 \text{ mV}$ and $P_i^{360} \approx 0.2 \text{ mW/cm}^2$. Figure 13(b) shows two cycles of the

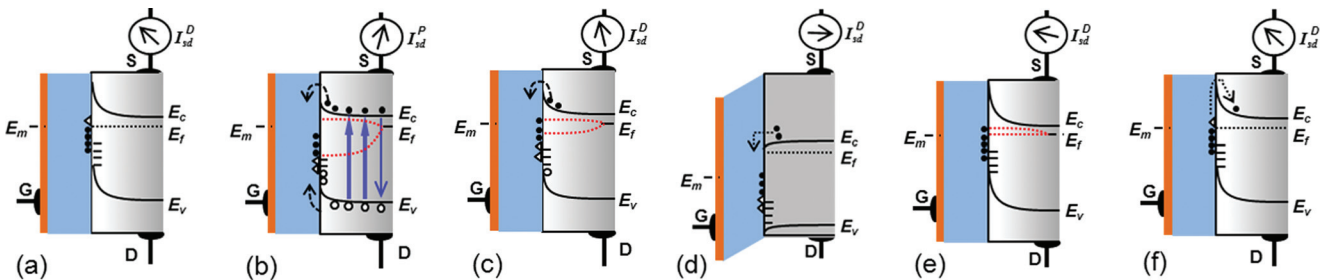


FIG. 12. Reset sequence for back-gated NW FET used as a photoconductive detector. Labels E_c , E_f , E_v and symbols for traps same as in Fig. 3. Gate oxide layer shaded in blue, gate contact labeled “G,” heavily doped Si substrate shaded in orange, Fermi level of the gate labeled “ E_m .” Relative values I_{sd}^D and I_{sd}^P in (a–d) indicated by schematic ammeter. Circuits associated with V_{sg} and V_{sd} not shown but it is understood that V_{sd} is constant throughout. Quasi Fermi levels for electrons and holes indicated schematically by dashed red lines. (a) Dark equilibrium, I_{sd}^D at its initial level, and $V_{sg} = 0$. (b) Device illuminated, I_{sd}^P now greater than I_{sd}^D in (a). (c) Device in dark, I_{sd}^D decays toward initial value in (a). (d) Device remains in dark, $V_{sg} < 0$, E_m pulled below E_f , electrons from quasi-neutral region of NW flood surface traps, I_{sd}^D rises above I_{sd}^D . (e) Device remains in dark, $V_{sg} = 0$, metastable surface traps filled in (d) now reside higher than E_f , SBB now greater and I_{sd}^D now less than respective values in (a). (f) Surface returns to equilibrium with bulk of NW, I_{sd}^D rises back to value in (a).

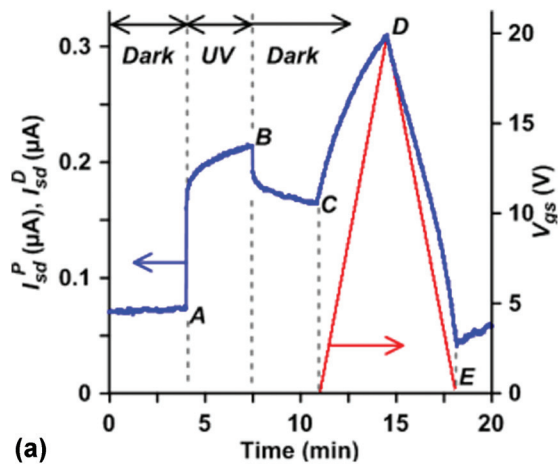
reset scheme superimposed upon PC/PPC excitation/decay data to illustrate that the reset procedure can rapidly restore I_{sd}^D to a level as low as or lower than what can be attained after roughly 20 h of passive photoconductive decay in the dark. The experimental results show the practical use of the reset method and support the plausibility of the model. Related gate-bias-induced transient surface charging phenomena in NW FET devices are discussed further in the following section.

V. ANALYSIS OF BACK-GATED FET DEVICES MAINTAINED IN THE DARK AND UNDER VACUUM

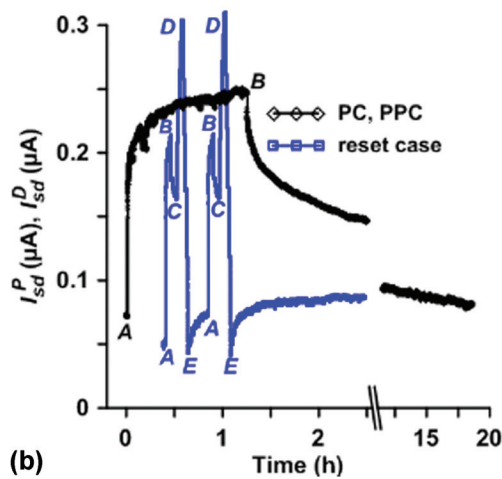
We also explored entirely electrical methods in efforts to deduce the assumed equilibrium surface charge density σ_s . In this work, a 3D Poisson solver applied to the ideal hexagonal NW cross section was used to model the measured depletion behavior for back-gated FET devices (operated in the dark and under vacuum) using the same assumed boundary condition described earlier, i.e., uniform fixed σ_s , uniform doping n_b determined separately by Raman analysis, complete donor ionization, and constant μ . These efforts are described in subsections VA–VC below.

A. Numerical fitting scheme for FET NW devices of hexagonal cross section

A cross-sectional schematic of the FET structure is illustrated in Fig. 14. The numerical fitting procedure was performed as follows. For respective values of $V_{sg} = V_{sg}^{(1,2)}$ corresponding to measured values of $I_{sd}^{D(1,2)}$ and computed integrated free charge densities $Q_i^{(1,2)}$, σ_s was iterated in the finite element solution procedure until the constraint $Q_i^{(1)}/Q_i^{(2)} = I_{sd}^{D(1)}/I_{sd}^{D(2)}$ was met. A representative example of this fitting procedure is illustrated in Figs. 15(a)–15(d) for sample 11 with $D_m = 128 \text{ nm}$, the NW resting on a 200 nm thick SiO_2 layer, and $n_b = 2.3 \times 10^{17} \text{ cm}^{-3}$. For gate voltages $V_{sg}^{(1,2)} = 0 \text{ V}, 5 \text{ V}$, the ratio $I_{sd}^{D(1)}/I_{sd}^{D(2)} \approx 1000:1$ and the solution $\sigma_s = 3.63 \times 10^{11} \text{ cm}^{-2}$ was found. Resulting graphs of V and n computed along a line parallel to $\langle 10\bar{1}0 \rangle$ passing through the NW center are given in Figs. 15(a) and 15(b), respectively, for the case of for $V_{sg}^{(1)} = 0 \text{ V}$. Figures 15(c)



(a)



(b)

FIG. 13. (a) One cycle of the reset sequence described in Figs. 12(a)–12(f) with I_{sd}^D and I_{sd}^P functions of time indicated in blue. Example is for sample 11 under vacuum with $V_{sd} = 50$ mV throughout. Device initially dwells in dark with $I_{sd}^D \approx 70$ nA as shown. I_{sd}^P initially rises quickly upon UV excitation at A with $P_i^{360} \approx 0.2$ mW/cm² and then slows as the competing processes to populate/depopulate surface traps and adsorb/desorb surface species come to equilibrium. The sample is returned to a dark state at B and I_{sd}^D begins to slowly decay. V_{gs} (red) begins to ramp up at C and I_{sd}^D correspondingly increases. V_{gs} and I_{sd}^D reach respective maximum values at D. The gate ramps down to $V_{gs} = 0$ at E whereupon the minimum value of I_{sd}^D is attained which is below the ≈ 70 nA level at the beginning of the cycle. Thereafter, I_{sd}^D drifts up toward this initial value. (b) Two cycles of the reset sequence (blue) compared with passive PC decay (black). The result shows that it requires roughly 20 h of passive decay to attain the same dark level and that can be reached far more rapidly by cycling the gate bias in the dark.

and 15(d) show the corresponding graphs of V and n for $V_{sg}^{(2)} = 5$ V.

B. Calculation of surface charge for “thin” devices

Figure 16(a) summarizes solutions for σ_s for “thin” devices (numbered per Table I) where D_m was in the range of roughly 74–129 nm. NWs within this span of diameters typically required $V_{sg} < 5$ V to deplete and displayed negligible drift in I_{sd}^D under sustained gate bias. Figure 16(b) illustrates this relatively drift-free depletion behavior for sample 9 with $D_m = 94$ nm with $V_{sg} = 2.4$ V. Note that the FET derived results for σ_s shown in Fig. 16(a) are roughly $2\times$ smaller

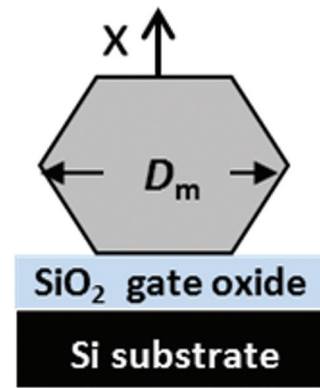


FIG. 14. Cross sectional schematic of back-gated FET structure simulated with finite-element Poisson solver.

than those found by saturated PC experiments given in Fig. 7(b).

C. Transient effects in “thick” devices

We now turn our attention to “thick” NW FET devices with D_m in the approximate range of 150–350 nm. FETs within this span of D_m typically required $V_{sg} > 10$ V to deplete with the thickest specimens requiring $V_{sg} > 100$ V. Devices requiring such elevated gate biases always displayed significant drift. Examples of the drift in I_{sd}^D under vacuum for a FET sample 16 with $D_m = 176$ nm are shown in Fig. 16(c). The numerical procedure for FET analysis applied to these thicker devices would not return solutions for σ_s that corresponded to measured ratios of I_{sd}^D even for $\sigma_s = 0$. This null result contradicts our initial assumption that a single charge specie is present on the NW surface and accounts for σ_s throughout the gate bias history of the device.

The experimental and numerical results suggest rather that the action of the depleting gate bias is to effectively inject free holes and/or fixed positive charge onto the surface of the NW in the vicinity of the gate electrode thereby partially screening the NW from the gate in a transient fashion. We propose the following mechanism which could account for such excess positive charge. As illustrated in Figs. 17(a) and 17(b), negatively charged traps (which are assumed to account for σ_s as described earlier) are pushed by the gate bias above the Fermi level of the NW. These traps emit electrons into the conduction band resulting in a net reduction of negative surface charge. At the same time, neutral midgap traps are pushed into the vicinity of the Fermi level. This enables Shockley-Read-Hall (SRH) emission (from the traps) of electrons into the conduction band and free holes into the valence band. Recall that the combined consequences of a trap located in a midgap position and at the Fermi level maximizes its probability of acting as an emission center.³³ Of course, such traps may exist as surface states or reside away from the surface but within the depletion region such that the relatively high value of V_{sg} still brings them into the vicinity of the Fermi level. In this scenario, free holes emitted from such traps accumulate near the surface at the valence band maximum and thus screen the gate in a transient fashion.

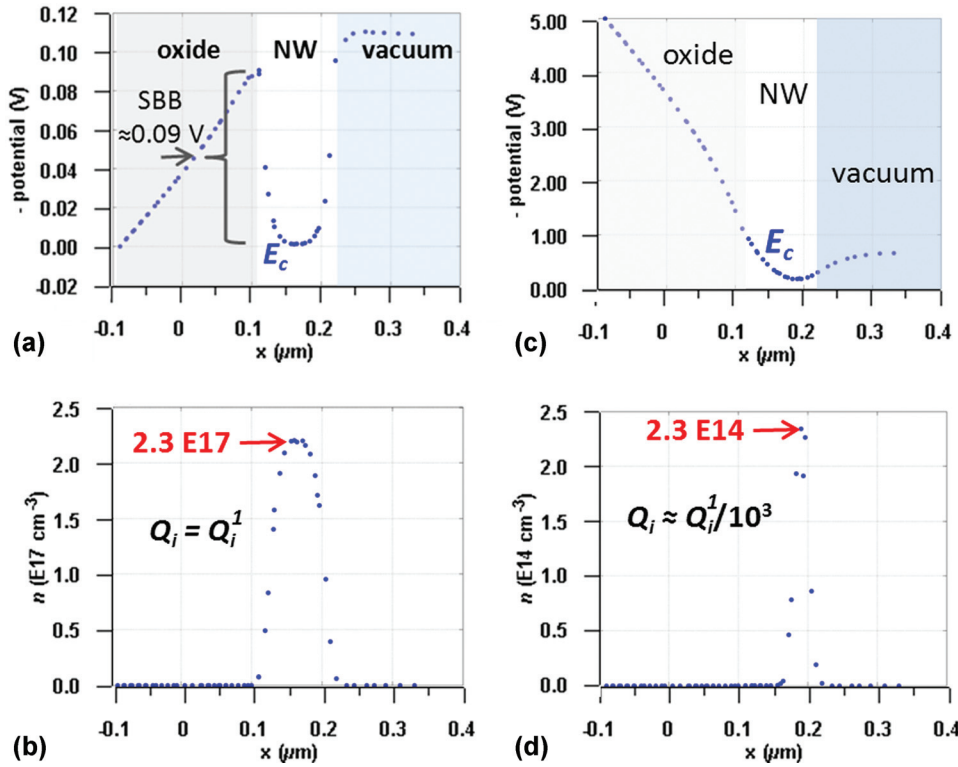


FIG. 15. Example result of finite-element computation of potential and free carrier concentration along x -axis (illustrated in Fig. 14) for sample 11 with $n_b = 2.3 \times 10^{17} \text{ cm}^{-3}$. For values of $V_{sg} = V_{sg}^{(1,2)} = 0, 5 \text{ V}$, corresponding to respective measured $I_{sd}^{D(1,2)}$, and computed integrated free charge densities $Q_i^{(1,2)}$, σ_s was iterated until the constraint $Q_i^{(1)}/Q_i^{(2)} = I_{sd}^{D(1)}/I_{sd}^{D(2)} = 10^3$ was met. This yielded $\sigma_s = 3.63 \times 10^{11} \text{ cm}^{-2}$. (a) With $V_{sg} = 0$, the graph displays V as a function of x through the oxide, NW, and into the vacuum. (b) Graph of n corresponding to (a). (c) V computed over same limits as (a) under depletion bias with $V_{sg} = 5 \text{ V}$. (d) Graph of n corresponding to (c).

VI. OTHER TRANSIENT FET PHENOMENA IN NW FET DEVICES

A. Optically induced transients in back-gated devices in vacuum and room air

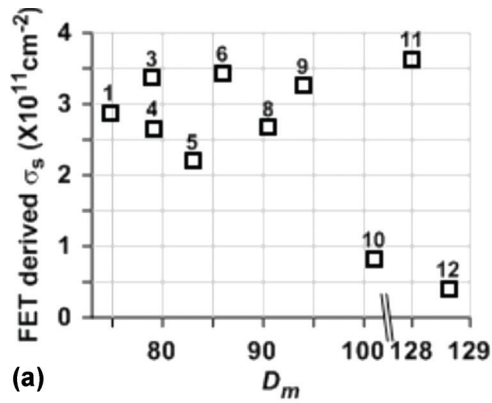
Optically induced changes to the surface charge, via mechanisms involving optically injected holes, or direct excitation of surface states, will also screen the gate in a NW FET. Consider the gate bias and illumination sequence illustrated in Fig. 18(a) for sample 19 (of batch B982) with $D_m = 372 \text{ nm}$, the sample under vacuum, and $V_{sd} = 1 \text{ mV}$ throughout. The sample was first subjected to one cycle of $V_{sg} = 100 \text{ V}$ for 10 min in the dark. Note the overshoot and decay in I_{sd}^D after $V_{sg} \rightarrow 0$ which suggests that excess positive charge near the gate is slowly returning to equilibrium. The sample was then illuminated continuously for 1 h at $P_i^{350} \approx 0.2 \text{ mW/cm}^2$ and then subjected to another cycle of $V_{sg} = 100 \text{ V}$. The data indicate that the FET is nearly immune to V_{sg} during UV exposure due to the population of photo-injected holes which accumulate in the vicinity of the gate.

As illustrated in Fig. 18(b), comparable behavior is observed when the same sample is examined in room air and illuminated at $\lambda = 550, 450, \text{ and } 360 \text{ nm}$ with $P_i^{\lambda} \approx 0.2 \text{ mW/cm}^2$ throughout. I_{sd}^D is lower than in vacuum as expected from Sec. IV and the requisite V_{sg} to deplete the device in the dark is correspondingly less. The data illustrate that as $\lambda \rightarrow 360 \text{ nm}$ the device becomes insensitive to the gate. Hence, both above-gap and sub-gap excitation can effectively screen the gate to varying degrees. To put this further into perspective, background room light at standard illumination levels will have roughly the same effect on the device in ambient air as the 550 nm case shown in Fig. 18(b).

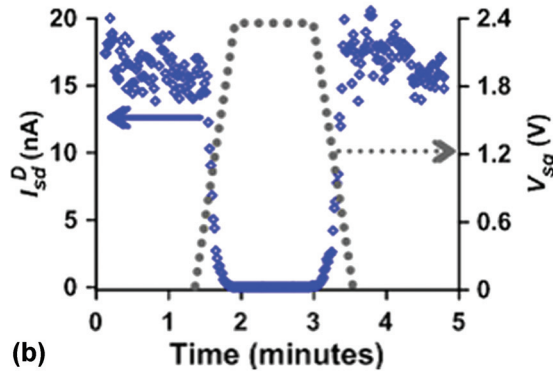
B. Back-gated FET drift transients in the dark under vacuum, room air, and dry air

We compared FET drift behavior under vacuum, room air, and dry air ambient conditions in order to draw some preliminary conclusions regarding the effect of water exposure. The dry air used in these experiments was specified as primarily N_2 with an O_2 fraction of 19.5%–23.5% and trace hydrocarbons at less than 1 PPM.³⁴ Figure 19(a) illustrates that prior to cycling V_{sg} , observe that I_{sd}^D is essentially equivalent under room air and dry air, but less than the vacuum case as expected from the prior discussion. The figure also shows that (aside from an offset of $\approx 50 \text{ nA}$) the I_{sd}^D transient for the vacuum and dry air ambients is comparable. However, the transient in room air is distinctly different from the dry air case. Figure 19(b) shows that as V_{sg} ramps up, I_{sd}^D in room air falls more rapidly than in dry air and attains a minimum at $V_{sg} \approx 80 \text{ V}$ in contrast to the dry air case even though both initially displayed equivalent I_{sd}^D for $V_{sg} = 0$.

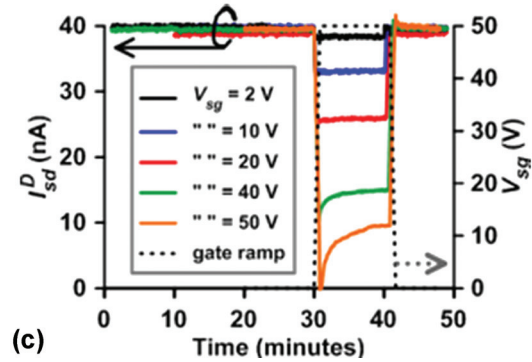
The FET behavior in room air suggests that there are two competing transient effects with different time constants occurring simultaneously under increasing and sustained V_{sg} . These are: (a) excess negative charge is attracted to the NW surface from the room air which results in depletion increasing more rapidly than under either the dry air or vacuum ambient conditions; (b) positive charge appears in the vicinity of the gate-NW interface which effectively screens the gate as described earlier. Eventually, the gate screening effects become dominant and I_{sd}^D drift up in a manner similar to both the dry air and vacuum cases. As illustrated in Fig. 19(a), with V_{sg} returned to zero, the behavior of room air transient in I_{sd}^D is consistent with both excess



(a)



(b)



(c)

FIG. 16. (a) Computation of σ_s for several devices using finite-element Poisson scheme as described in the text. Numbered elements on graph correspond to samples listed in Table I. (b) Depletion behavior of sample 9 with $V_{sd} = 100$ mV. (c) Depletion behavior sample 16 with $V_{sd} = 100$ mV and V_{sg} dwelled at successively greater values.

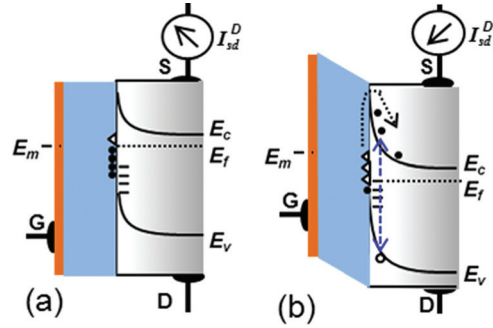


FIG. 17. Schematic of back-gated FET illustrating transient drift in I_{sd}^D under sustained V_{sd} and V_{sg} . (a) Steady-state dark depletion conditions with $V_{sg} = 0$ and constant V_{sd} producing I_{sd}^D . (b) Device is biased into depletion with $V_{sg} > 0$, I_{sd}^D initially falls below value in (a). Initially filled surface traps now pushed above E_f by gate bias and emit electrons into conduction band, near-midgap neutral traps pushed into coincidence with E_f thus increasing probability of hole emission into valence band and electron emission into conduction band. Gate becomes screened and I_{sd}^D drifts up.

positive charge returning to equilibrium within the NW and excess negative charge being released from the NW surface. Note also the room air and dry air transients converge to a common I_{sd}^D roughly 1 h after $V_{sg} \rightarrow 0$.

C. FET transients in Schottky-gated nanowire MESFET devices

It is interesting to compare the prior results concerning back-gated FETs with NW MESFET devices. Since the latter employ Schottky contacts to form the gate, one might expect that under sustained depletion bias the I_{sd}^D transients would be consistent with the accumulation of excess negative charge supplied by the reverse saturation current flowing into the Schottky contact and thus result in transient behavior which is opposite to that observed with the back-gated devices. We indeed observe that this trend is the case as described next.

Consider the “omega-gate” MESFET depicted in Fig. 2(b). We reported fabrication and operational details of such devices elsewhere.¹⁷ Figure 20 shows the I_{sd}^D transients for sample 21 recorded under vacuum for various examples of sustained V_{sg} . Observe that I_{sd}^D drifts downward for cases where the gate bias dwelled at constant values with

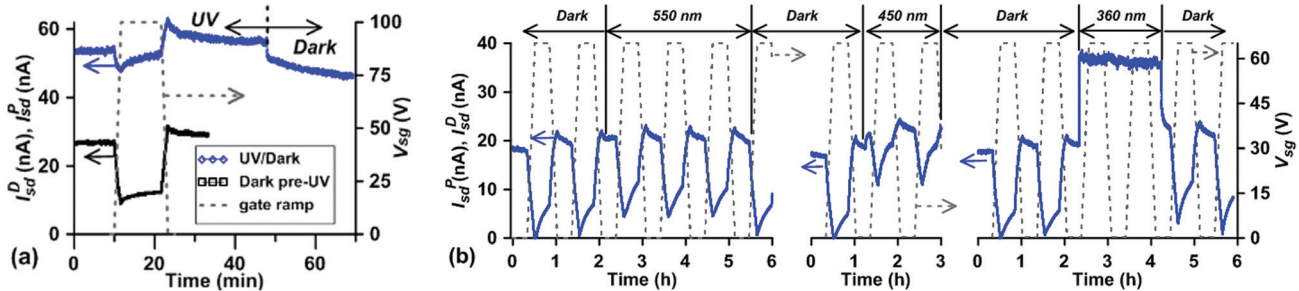


FIG. 18. Comparative FET gate screening effects induced by UV-visible illumination in sample 19 under vacuum and in room air with $V_{sd} = 1$ mV. (a) Black curve: I_{sd}^D with sample in dark while sweeping a single gate-bias cycle with $0 \text{ V} \leq V_{sg} \leq 100 \text{ V}$. Blue curve: I_{sd}^P with $P_i^{360} \approx 0.2 \text{ mW/cm}^2$ while sweeping V_{sg} over same range as (a). After 10 min of sustained $V_{sg} = 100 \text{ V}$ under UV illumination, I_{sd}^P has nearly drifted up to its initial value at $V_{sg} = 0 \text{ V}$. Sample returned to dark after roughly 50 min and I_{sd}^D decays slowly. (b) I_{sd}^D and I_{sd}^P in room air in the dark, and illuminated at $\lambda = 550 \text{ nm}$, 450 nm , and 360 nm during gate cycling with $0 \text{ V} \leq V_{sg} \leq 60 \text{ V}$. $P_i^{\lambda} \approx 0.2 \text{ mW/cm}^2$ throughout. In this case, I_{sd}^D , and requisite V_{sg} for depletion, are lower than in (a) due to the increased ϕ in the room air ambient. The sample displays progressively reduced sensitivity to the gate bias with decreasing λ and is immune to the gate with $\lambda = 360 \text{ nm}$.

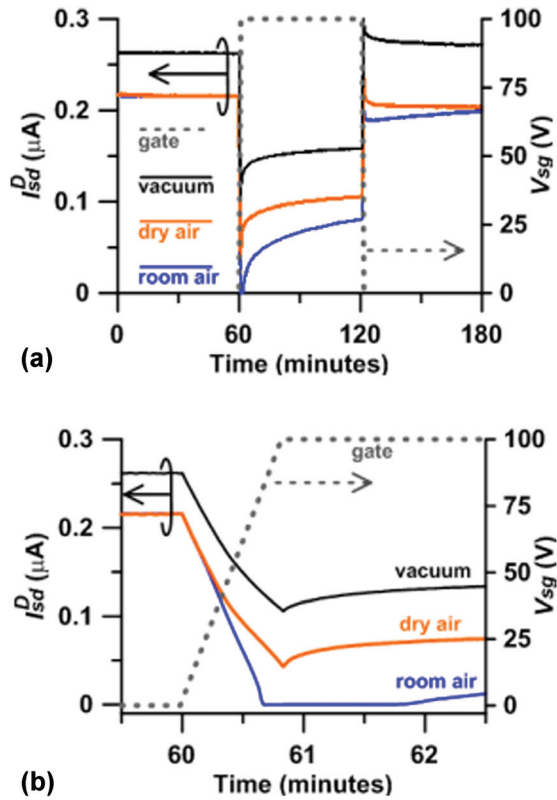


FIG. 19. Comparative I_{sd}^D transient behavior for sample 18 with $V_{sd}=7$ mV and $0V \leq V_{sg} \leq 100V$ under vacuum, dry air, and room air. (a) Both air ambients result in the same value of I_{sd}^D while I_{sd}^D under vacuum is larger as expected from prior examples. Except for an offset in I_{sd}^D , the transient behaviors under vacuum and dry air are nearly identical with one another but distinctly different from the case under room air. (b) Detail of I_{sd}^D transients for the 3 cases as V_{sg} ramps up. Note that the case under room air depletes at a comparatively greater rate.

$V_{sg} > 3$ V. With V_{sg} returned to zero, I_{sd}^D comes up to a level that is initially less than what was observed prior to the sustained application of V_{sg} , which is consistent with metastable storage of negative charge on the surface.

VII. DISCUSSION

As illustrated in Fig. 6(b), the consequences of propagating the estimated uncertainties in D_m and n_b result in a fairly large uncertainty and span in our results for μ . Considering all the samples examined, we find (approximately) that $800 \text{ cm}^2/(\text{V s}) < \mu < 2100 \text{ cm}^2/(\text{V s})$. This range of μ is nonetheless consistent with the theoretical and experimental reports GaN within the doping levels considered herein.³⁵ Furthermore, this range of μ also overlaps with the $820 \pm 120 \text{ cm}^2/(\text{V s})$ value obtained via non-contact THz photoconductivity (applied to Batch 982) as recently reported.³⁶ We also remark that there can be apparent UV-induced desorption/adsorption drift in I_{sd}^S (roughly 5%–10%) in vacuum under the intense 325 nm excitation. For consistency, we generally let the photocurrent stabilize for a few minutes before recording I_{sd}^S . These effects likely contribute to the scatter in μ observed between samples. Furthermore, if this procedure consistently *underestimated* the saturation photocurrent, then our result for μ would be correspondingly less.

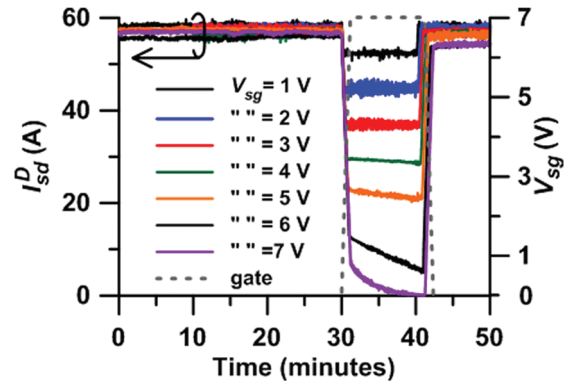


FIG. 20. Comparative I_{sd}^D transient behavior for (MESFET) sample 21 with $V_{sd}=3$ mV. The device depletes at lower values of V_{sg} (compared to prior back-gated device examples) because the gate geometry is more efficient and the doping density is lower. The behavior of the transient response suggests excess negative charge is accumulating on the NW surface as a likely result of the reverse saturation current flowing through the reverse-biased Schottky contact.

Even with the estimated uncertainties in D_m , μ , and n_b considered, the results of the depletion analysis using the cylindrical Poisson solver applied to the values of I_{sd}^D recovers a span for ϕ that falls within the (0.2 ± 0.1) eV range deduced by XPS. Furthermore, our XPS results for $E_f - E_v$ are consistent with independent work on air-exposed MBE grown GaN films.³⁷ Of course, our XPS and Poisson-derived results for ϕ are not completely independent since the Raman-derived n_b is implicitly used in the determination of both. We also acknowledged in Refs. 11 and 25 that other researchers often find larger values of ϕ for GaN films than our results suggest.

We note that our estimated range of ϕ is also consistent with our prior PC work and that of other researchers.^{7,8,11,13,38} However, these comparisons require further context since the NWs studied encompassed a wide range of n_b as follows:

- In Ref. 11, we showed NWs with $n_b \approx (3-6) \times 10^{16} \text{ cm}^{-3}$ yielded $\phi \approx (0.2-0.3)$ eV.
- MBE *c*-axis NW batches with $n_b = 6.25 \times 10^{17} \text{ cm}^{-3}$ and $1.8 \times 10^{18} \text{ cm}^{-3}$ are described in Refs. 7 and 8 which also report $\phi \approx 0.55$ eV. This estimate for ϕ was apparently justified by the XPS result for ϕ_s of Ref. 37 which was measured on MBE GaN films that were examined *prior* to air exposure. If we instead use the results for Ref. 37 reported for *air exposed* GaN, and assume the values of n_b of Refs. 7 and 8 are correct, we then estimate $\phi \approx 0.3$ eV rather than 0.55 eV for their results. Note that our XPS result for ϕ_s measured after *in-situ* plasma cleaning and annealing of GaN NWs agrees with the Ref. 37 result for the case of an MBE GaN film measured prior to air exposure.
- Studies of *m*-axis NWs with $N \approx 10^{18} \text{ cm}^{-3}$ reportedly yielded $\phi = 0.226$ eV.³⁸
- As just described in (a-c) above, such similar values of ϕ over a wide range of n_b suggest a distribution of surface traps with energy in the vicinity of 0.3 eV below E_c at the surface. This effect is illustrated with the hypothetical room temperature example of a single (dominant)

surface state at energy E_{ss} in thermal equilibrium with a planar n -type GaN film.³⁹ We approach the solution to this problem in a manner as given by Mönch.⁴⁰ In Fig. 21, we show simulations which illustrate ϕ and $(E_{ss} - E_f)$ as a function of surface state density (n_{ss}) with $(E_c - E_{ss}) = 0.35$ eV (at the surface) for Si-doped GaN for cases with $n_b = 4.6 \times 10^{16} \text{ cm}^{-3}$, $1.9 \times 10^{17} \text{ cm}^{-3}$, and $6.1 \times 10^{17} \text{ cm}^{-3}$. For all three cases of n_b , ϕ falls into the range of (0.2–0.3) eV for n_{ss} in the range of $(1\text{--}2) \times 10^{12} \text{ cm}^{-2}$. This estimated range of n_{ss} is consistent with our observed PC saturation conditions (both herein and Ref. 11) since the surface density of photo-generated holes is $\approx 1 \times 10^{12} \text{ cm}^{-2}$ at the maximum P_i^{325} available.

Our assertion that SBB is reduced via the desorption of oxygen under vacuum and by UV exposure is consistent with reports of other workers.^{12,16,19,30} Furthermore, the PC decay rate under vacuum appears to be longer than in air in concurrence with Ref. 12. This behavior suggests the accelerated PC decay in air that occurs upon switching off the UV excitation occurs because the oxygen-desorbed surface immediately begins to take up oxygen from the ambient environment. This re-adsorption process hastens the PC decay by providing an additional pathway for the SBB to recover besides the assumed repopulation of surface traps by electrons thermally excited from the interior of the NW. We also observed that the increased NW conductivity under vacuum compared to air is akin the increased conductivity we reported for NWs coated with Al_2O_3 via atomic layer deposition (ALD).¹¹ Comparing the results suggests a mechanism where residual adsorbed oxygen on the NW surface is scavenged by the ALD process during the formation of the Al_2O_3 thus decreasing the SBB of the NW. By contrast, ALD deposition of TaN films showed only modest changes to the NW conductivity.¹¹

The drift behavior of back-gated NW FET devices biased into partial or full depletion, even under vacuum and in

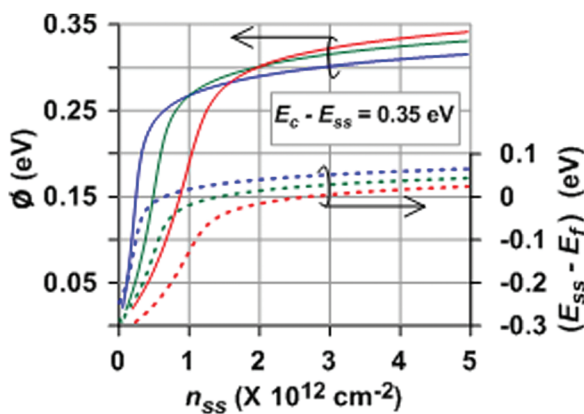


FIG. 21. Example of room temperature surface band bending ϕ as a function of surface state density n_{ss} for the hypothetical case of a thin Si:GaN film with respective doping levels $n_b = 4.6 \times 10^{16}$ (blue solid), 1.9×10^{17} (green solid), and $6.1 \times 10^{17} \text{ cm}^{-3}$ (red solid). Also shown in dashed lines of same respective colors and values of n_b are the offsets of the surface state from the Fermi level. The results are computed for a single surface state with $(E_c - E_{ss}) = 0.35$ eV (at the surface) and illustrates that ϕ falls into the range of 0.2–0.3 eV for $n_{ss} = 1\text{--}2 \times 10^{12} \text{ cm}^{-2}$ for all three values of n_b .

the dark, illustrates the difficulty in determining NW transport properties by purely electrical means.^{10,41} The experimental and numerical results suggested that the action of the sustained gate bias was to inject positive charge into the vicinity of the gate-NW interface thereby effectively screening the channel region of the FET from the gate. The transient artifacts in I_{sd}^D rendered static FET simulations of limited value for estimating σ_s in devices requiring $V_{sg} > 5$ V to deplete. Similar transient artifacts in back-gated NW FETs that were also ascribed to injection of positive charge have been described by Simpkins *et al.*⁴¹ As discussed earlier and in Fig. 17, we offer a plausibility argument to account for the injection of free holes that assumes SRH emission from midgap traps that are elevated to the vicinity of the Fermi level by sufficiently high V_{sg} .

Transient drift effects of back-gated FETs in the dark under ambient air, dry air, and vacuum were compared. Except for an offset in I_{sd}^D (with $V_{sg} = 0$), the qualitative behavior under vacuum and dry air was nearly identical. However, the transient device operation under ambient air was different. FET drift in ambient air suggests such gate-bias-induced artifacts as adsorption/desorption of water and/or OH species, or circumferential electro-migration around the NW surface of weakly bound charged adsorbates. In consideration of the adsorption/desorption scenario, Wang *et al.* (Ref. 42) have recently demonstrated a NW photocatalyst process whereby photogenerated holes accumulating on m -plane surfaces of MBE grown c -axis NWs will evolve O_2 from adsorbed water. Hence, if the gate-bias hole-injection scheme described earlier is correct, holes accumulating on the exposed NW surface near the intersection with the gate oxide would evolve oxygen via splitting water that was adsorbed onto the NW surface from the ambient air. Such evolved oxygen would then be available to adsorb onto the NW surface thus increasing depletion in a transient fashion.

Optically induced gate-screening artifacts in back-gated FETs were also described, both in room air and under vacuum. Although these effects were most pronounced with above-gap excitation, they were still measurable even at 600 nm illumination under comparable intensities ($\sim 0.2 \text{ mW/cm}^2$). Such behavior is anticipated by considering the spectral dependence of the PC illustrated in Figs. 10(a) and 10(b) where a rapidly diminishing, but featureless, PC sensitivity was observed as the excitation wavelength increased from 360 nm into the visible. These observations suggest that while the dominant optically induced gate-screening effect is due to above-gap photogenerated holes, sub-gap excitation of defect, trap, or surface states also play a role. Furthermore, the similarity of the photo-induced and dark FET transients lend credence to the argument that hole emission indeed occurs under sustained depletion bias. Finally, it is also instructive to note that effects of optically induced hole injection in perturbing depletion layers have been treated analytically for specialized cases.⁴³

Although back-gate and optically induced transient artifacts can be troublesome in FET operation, simulations, and open to considerable debate, we showed that such effects can nevertheless be exploited to rapidly reset the dark state of a NW photoconductive detector. In the present discussion, we

only implement a proof-of-principle demonstration of the concept. Further engineering development of this approach is deferred to later work.

Finally, we found that the drift behavior of Schottky-gated MESFETs under vacuum in the dark was in the opposite sense of the back-gated devices but displayed comparable temporal evolution. This result is consistent with the view that the reverse saturation current flowing into the Schottky contact is contributing transient excess negative charge onto the NW surface thus producing a transient increase in depletion under sustained gate bias.

VIII. CONCLUSIONS

Combined experimental efforts in photoconductivity, Raman scattering, and XPS were applied to studies of transport properties in MBE grown GaN nanowires. Measurements were performed in vacuum and ambient air. For *n*-type samples with free carrier concentration in the low- 10^{17} cm $^{-3}$, the drift mobility fell into the range 800 cm 2 /(V s) $< \mu < 2100$ cm 2 /(V s), the SBB was $\varnothing = (0.2 \pm 0.1)$ eV, and the negative surface charge density assumed responsible for the SBB was in the range 3.5×10^{-11} cm $^{-2} < \sigma_s < 7.5 \times 10^{-11}$ cm $^{-2}$. Back-gated NW FET devices (in the dark) that required $V_{sg} < 5$ V to deplete generally returned values of σ_s that were on average $\approx 2\times$ less than the photoconductivity-derived results. Back-gated FET devices under illumination behaved in a manner consistent with photo-injected holes screening the gate. The drift behavior of the same devices in the dark was consistent with gate screening via electrically injected holes and/or electrically induced emission of trapped electrons from surface states. The dark drift behavior of NW MESFET devices was opposite that of back-gated devices. Finally, FET gate-transient artifacts were used to accelerate the otherwise long recovery time of NW photoconductive detectors.

ACKNOWLEDGMENTS

We gratefully acknowledge R. Nemanich for use of the ASU Nanoscience Laboratory, and fruitful discussions with S. King of Intel Corporation. Additionally, we have benefited from discussions with M. Brubaker, A. Davydov, A. Motayed, and A. Roshko (all with NIST).

APPENDIX: METHOD FOR ESTIMATING DIAMETER-DEPENDENCE OF DRIFT MOBILITY

We assume a low-field condition where an electron is isotropically scattered and that scattering is equally likely at any point within the nanowire. In a bulk semiconductor, the possible trajectories traversed between scattering events occupy a spherical region. Averaging over all possible trajectories yields the bulk mean free path (λ_B). If the starting point of a trajectory is sufficiently near the surface in a NW, then scattering will occur at a range less than λ_B . We averaged over all possible starting points in the cross-section of a nanowire of circular cross section and calculated the separation between scattering events, i.e., the diameter-dependent

mean-free path λ_{NW} . Defining τ , v_{th} , and m_n as the average time between scattering events, the electron thermal velocity, and the effective mass of a conduction band electron, respectively, then $\lambda_{NW} = \tau v_{th}$ where $v_{th} = \sqrt{8kT/\pi m_n}$. With $\mu = q\tau/m_n$ and $m_n = 0.2 m_e$, we find that for a bulk value of $\mu = 1400$ cm 2 /(V s) (corresponding to roughly the mean value of μ as displayed in Fig. 6(b)) the diameter-dependent value of μ will fall to approximately 75% of this bulk value for $D_A \approx 76$ nm. However, since this is at or near the lower limit of D_A for the samples available, it is unlikely that the diameter dependence of μ need be considered in the present discussion.

¹K. A. Bertness, N. A. Sanford, and A. V. Davydov, *IEEE J. Sel. Top. Quantum Electron* **17**, 847 (2011).

²T. Stoica and R. Calarco, *IEEE J. Sel. Top. Quantum Electron* **17**, 859 (2011).

³S. Li and A. Waag, *J. Appl. Phys.* **111**, 071101 (2012).

⁴G. S. Aluri, A. Motayed, A. V. Davydov, V. P. Oleshko, K. A. Bertness, N. A. Sanford, and R. V. Mulpuri, *Nanotechnology* **23**, 175501 (2012).

⁵See <http://www.glo.se> for Glö AB.

⁶A. A. Talin, B. S. Swartzentruber, F. Léonard, X. Wang, and S. D. Hersee, *J. Vac. Sci. Technol. B* **27**(4), 2040 (2009).

⁷R. Calarco, M. Marso, T. Richter, A. I. Aykanat, R. Meijers, A. v. d. Hart, T. Stoica, and H. Lüth, *Nano Lett.* **5**, 981 (2005).

⁸T. Richter, H. Lüth, R. Meijers, R. Calarco, and M. Marso, *Nano Lett.* **8**, 3056 (2008).

⁹B. S. Simpkins, M. A. Mastro, C. R. Eddy, Jr., and P. E. Pehrsson, *J. Appl. Phys.* **103**, 104313 (2008).

¹⁰L. M. Mansfield, K. A. Bertness, P. T. Blanchard, T. E. Harvey, A. W. Sanders, and N. A. Sanford, *J. Electron. Mater.* **38**, 495 (2009).

¹¹N. A. Sanford, P. T. Blanchard, K. A. Bertness, L. Mansfield, A. W. Sanders, A. Roshko, B. B. Burton, and S. M. George, *J. Appl. Phys.* **107**, 0343318 (2010). Note that for sample batch B738 described, the estimate free carrier concentration of $(3-6) \times 10^{16}$ cm $^{-3}$ is corroborated within uncertainty by subsequent Raman analysis (Ref. 24 herein) which yielded $(7.0 \pm 1.2) \times 10^{16}$ cm $^{-3}$.

¹²M. Kang, J.-S. Lee, S.-K. Sim, H. Kim, B. Min, K. Cho, G.-T. Kim, M.-Y. Sung, S. Kim, and H. S. Han, *Jpn. J. Appl. Phys., Part 1* **43**, 6868 (2004).

¹³R.-S. Chen, H.-Y. Chen, C.-Y. Lu, K.-H. Chen, C.-P. Chen, L.-C. Chen, and Y.-J. Yang, *Appl. Phys. Lett.* **91**, 223106 (2007).

¹⁴J. B. Schlager, K. A. Bertness, P. Blanchard, L. H. Robins, A. Roshko, and N. A. Sanford, *J. Appl. Phys.* **103**, 124309 (2008).

¹⁵J. B. Schlager, N. A. Sanford, K. A. Bertness, and A. Roshko, *J. Appl. Phys.* **109**, 044312 (2011).

¹⁶C. Pfüller, O. Brandt, F. Grosse, T. Flissikowski, C. Chèze, V. Consonni, L. Geelhaar, H. T. Grahn, and H. Riechert, *Phys. Rev. B* **82**, 045320 (2010).

¹⁷P. T. Blanchard, K. A. Bertness, T. E. Harvey, L. M. Mansfield, A. W. Sanders, and N. A. Sanford, *IEEE Trans. Nanotechnol.* **7**, 760 (2008).

¹⁸P. T. Blanchard, K. A. Bertness, T. E. Harvey, A. W. Sanders, N. A. Sanford, S. M. George, and D. Seghete, *IEEE Trans. Nanotechnol.* **11**, 479 (2012).

¹⁹R. S. Chen, C. Y. Lu, K. H. Chen, and L. C. Chen, *Appl. Phys. Lett.* **95**, 233119 (2009).

²⁰K. A. Bertness, A. Roshko, L. M. Mansfield, T. E. Harvey, and N. A. Sanford, *J. Cryst. Growth* **310**, 3154 (2008).

²¹A. W. Sanders, P. Blanchard, L. Robins, N. Sanford, K. Bertness, and G. Wang, in 54th Annual Electronics Materials Conference, 20-22 June, 2012, Pennsylvania State University, University Park, PA, paper II. In these experiments, the scanning nanoprobe would only assess roughly 70%–80% of the NW length because one end of the NW was anchored under an ohmic contact.

²²A. Many, Y. Goldstein, and N. B. Grover, *Semiconductor Surfaces* (North-Holland, Amsterdam, 1965), p. 138; D. R. Frankl, *Electrical Properties of Semiconductor Surfaces* (Pergamon Press, Oxford, 1967), p. 42. 244.

²³C.-E. Fröberg, *Introduction to Numerical Analysis* (Addison-Wesley, Reading, MA, 1965), p. 244.

²⁴L. H. Robins, N. A. Sanford, K. A. Bertness, and J. B. Schlager, in 2012 MRS Spring Meeting, 9–13 April, 2012, San Francisco, CA, poster AA 6.19.

²⁵J. Yang, B. S. Eller, C. Zhu, C. England, and R. J. Nemanich, *J. Appl. Phys.* **112**, 053710 (2012).

- ²⁶J. R. Walrop and R. W. Grant, *Appl. Phys. Lett.* **68**, 2879 (1996).
- ²⁷J. P. McKelvey, *Solid State and Semiconductor Physics* (Harper and Row, New York, 1966), p. 276. See also Ref. 35.
- ²⁸S. Han, W. Jin, D. Zhang, T. Tang, C. Li, X. Liu, Z. Liu, B. Lei, and C. Zhou, *Chem. Phys. Lett.* **389**, 176 (2004).
- ²⁹F. González-Posada, R. Songmuang, M. Den Hertog, and E. Monroy, *Nano Lett.* **12**, 172 (2012).
- ³⁰M. A. Reshchikov, M. Foussekis, and A. A. Baski, *J. Appl. Phys.* **107**, 113535 (2010).
- ³¹A. Armstrong, Q. Li, Y. Lin, A. A. Talin, and G. T. Wang, *Appl. Phys. Lett.* **96**, 163106 (2010).
- ³²L. Kronik and Y. Shapira, *Surf. Sci. Rep.* **37**, 1 (1999).
- ³³E. H. Nicolian and J. R. Brews, *MOS (Metal Oxide Semiconductor) Physics and Technology* (John Wiley, New York, 1982).
- ³⁴General Air product specification data for “air zero” dry air.
- ³⁵H. Morkoc, *Nitride Semiconductors and Devices* (Springer-Verlag, Berlin, 1999).
- ³⁶P. Parkinson, C. Dodson, H. J. Joyce, K. A. Bertness, N. A. Sanford, L. M. Herz, and M. B. Johnston, *Nano Lett.* **12**, 4600 (2012).
- ³⁷M. Kočan, A. Rizzi, H. Lüth, S. Keller, and U. K. Mishra, *Phys. Status Solidi B* **234**, 773 (2002).
- ³⁸H.-Y. Chen, R.-S. Chen, N. K. Rajan, F.-C. Chang, L.-C. Chen, K.-H. Chen, Y.-J. Yang, and M. A. Reed, *Phys. Rev. B* **84**, 205443 (2011). The free carrier concentration of the samples used in this study was estimated to be roughly 10^{18} cm^{-3} , M. A. Reed, private communication (2012).
- ³⁹S. Chevtchenko, X. Ni, Q. Fan, A. A. Baski, and H. Morkoc, *Appl. Phys. Lett.* **88**, 122104 (2006).
- ⁴⁰W. Mönch, *Semiconductor Surfaces and Interfaces, Third Edition* (Springer-Verlag, Berlin, 2001), pp. 61–62. In this approach, note that to a good approximation one may ignore the donor ionization energy since, due to the upward band bending, the donors are fully ionized throughout nearly the entire space charge region.
- ⁴¹B. S. Simpkins, M. A. Mastro, C. R. Eddy, Jr., and P. E. Pehrsson, *J. Phys. Chem. C* **113**, 9480 (2009).
- ⁴²D. Wang, A. Pierre, M. G. Kibria, K. Cui, X. Han, K. H. Bevan, H. Guo, S. Paradis, A.-R. Hakima, and Z. Mi, *Nano Lett.* **11**, 2353 (2011).
- ⁴³J. L. Moll, *Physics of Semiconductors* (McGrall-Hill, New York, 1964), p. 264.